

## Halo formation and chaos in root-mean-square matched beams propagating through a periodic solenoidal focusing channel

Y. Fink and C. Chen

*Plasma Science and Fusion Center, Massachusetts Institute of Technology, Cambridge, Massachusetts 02139*

W. P. Marable

*Department of Mathematics, Hampton University, Hampton, Virginia 23668*

(Received 24 September 1996; revised manuscript received 20 February 1997)

The dynamics of continuous space-charge-dominated beams propagating through a periodic solenoidal focusing channel is studied using a test-particle model. It is shown that nonlinearities in the self-fields induce chaotic particle motion and beam halo formation for beams that are root-mean-square matched into the focusing channel but have nonuniform density profiles transverse to the direction of beam propagation. In particular, two parabolic density profiles are considered. For beams with hollow density profiles, it is found that excessive space charge at the edge of the beam induces two pairs of stable and unstable period-one orbits in the vicinity of the beam core envelope, and that the chaotic layer associated with the unstable period-one orbits allows particles to escape from the core to form a halo. On the other hand, for beams with hump density profiles (i.e., with high densities on the beam axis and low densities at the beam edge), it is found that excessive space charge on the beam axis induces an unstable fixed point on the axis and two stable period-one orbits off the axis inside the beam, and that the chaotic layer associated with the unstable fixed point is responsible for halo formation. In both cases, the halo is found to be bounded by a Kolmogorov-Arnold-Moser surface. The ratio of halo to beam core envelope is determined numerically. [S1063-651X(97)07106-7]

PACS number(s): 29.27.-a, 41.75.-i, 41.85.-p

### I. INTRODUCTION

Beam halo formation is an important issue in the design and development of next generation high-power particle accelerators and high-power microwave and millimeter wave tubes for a wide range of applications such as high-energy and nuclear physics research, accelerator production of tritium, heavy ion fusion, and high-power, high-resolution radar [1]. Depending upon the application, beam halos, if not controlled, can lead to intolerable beam losses, radio-frequency (rf) breakdown, radioactivity buildup in the accelerator, and emittance growth, to mention a few examples. It has been recognized recently [2–9] that for space-charge-dominated beams, halo formation is due to chaotic beam dynamics induced by nonlinear space-charge effects. Chaotic particle orbits not only are *sensitive to initial conditions*, but also occupy a larger region in phase space than regular particle orbits, resulting in beam halo formation and growth in the total (edge) emittance.

In this paper, we explore the mechanisms of chaotic behavior and halo formation in continuous, space-charge-dominated beams propagating through a periodic solenoidal focusing channel with well matched root-mean-square (rms) beam envelopes. For a periodic solenoidal focusing channel with the periodicity length  $S$  and the vacuum phase advance  $\sigma_0$ , a *space-charge-dominated beam* satisfies the condition [9]

$$\frac{SK}{4\sigma_0\epsilon} > 1,$$

whereas an *emittance-dominated beam* satisfies the condition

$$\frac{SK}{4\sigma_0\epsilon} \ll 1.$$

Here,  $K = 2\nu/\gamma_b^3\beta_b^2$  is the normalized beam perveance,  $\epsilon$  is the unnormalized rms emittance of the beam [10],  $\nu$  is the Budker parameter, and  $\beta_b c$  and  $\gamma_b$  are the (average) velocity and relativistic mass factor of the particles, respectively. For an electron beam,

$$\frac{SK}{4\sigma_0\epsilon} = 2.9 \times 10^{-5} \frac{1}{\sigma_0} \left( \frac{S}{\epsilon_n} \right) \frac{I_b}{\gamma_b^2\beta_b^2},$$

where  $I_b$  is the electron beam current in amperes,  $\epsilon_n = \gamma_b\beta_b\epsilon$  is the normalized rms emittance in meter-rad, and  $S$  is in meters. For an ion beam,

$$\frac{SK}{4\sigma_0\epsilon} = 1.6 \times 10^{-8} \frac{1}{\sigma_0 A} \left( \frac{q}{e} \right) \left( \frac{S}{\epsilon_n} \right) \frac{I_b}{\gamma_b^2\beta_b^2},$$

where  $A$  and  $q/e$  are the atomic mass and magnitude of the charge state of the ion, respectively,  $I_b$  is the ion beam current in amperes,  $\epsilon_n = \gamma_b\beta_b\epsilon$  is the normalized rms emittance in meter-rad, and  $S$  is in meters.

In particular, use is made of a test-particle model to show that nonlinearities in the self-fields induce chaotic particle motion and beam halo formation. This analysis pertains to beams that are rms matched into the focusing channel but have nonuniform density profiles transverse to the direction of beam propagation. Two parabolic density profiles are considered. For beams with hollow density profiles (i.e., with low densities on the beam axis and high densities at the beam edge), it is found that excessive space charge at the edge of

the beam induces two pairs stable and unstable period-one orbits in the vicinity of the beam core, and that the chaotic layer associated with the unstable period-one orbits allows particles to escape from the core to form a halo. These results agree qualitatively with recent experimental observations of halo formation in a potassium ( $K^+$ ) ion beam in the 2-MV Heavy Ion Injector Experiment at Lawrence Berkeley National Laboratory (LBNL), where the core of the beam has a sharp-edged hollow density profile [11]. On the other hand, for beams with hump density profiles (i.e., with high densities on the beam axis and low densities at the beam edge), it is found that excessive space charge at the beam axis induces an unstable fixed point on the axis and two stable period-one orbits off the axis inside the beam, and that the chaotic layer associated with the unstable fixed point is responsible for halo formation. In both cases, the halo is found to be bounded by a Kolmogorov-Arnold-Moser (KAM) surface [12]. The ratio of halo to beam core envelope is determined numerically.

Results presented in this paper are qualitatively the same as those obtained previously for rms-matched beam propagation through an alternating-gradient quadrupole magnetic focusing channel [4]. An important conclusion from the present analysis is that the reported chaotic behavior and beam halo formation occur, regardless of whether the beam has an elliptical or circular cross section.

The organization of this paper is as follows. In Sec. II, we present a test-particle model for studies of the dynamics of rms-matched beams with a parabolic density profile. The beam envelope equation is derived following the work by Sacherer [10], and is used to determine the core radius of the rms-matched beam. The equations of motion are derived for test particles. A distribution function, which is consistent with the assumed parabolic density profile and that also approaches the Kapchinskij-Vladimirskij (KV) distribution [13] continuously as the density becomes uniform, is employed in order to specify the initial conditions of the test particles. In Sec. III, the effects of space charge on the dynamics of a KV beam are illustrated in the context of the present test-particle analysis. The Poincaré surface-of-section technique [12] is used to study the test-particle motion under the influence of the nonlinear self-fields associated with the charge density nonuniformity, including chaotic particle motion and associated processes of halo formation. Finally, conclusions are drawn in Sec. IV.

## II. MODEL AND ASSUMPTIONS

We consider an intense, continuous charged-particle beam propagating at axial velocity  $\beta_b c \hat{e}_z$  through a periodic solenoidal focusing channel, as shown schematically in Fig. 1. In the thin-beam approximation, the applied magnetic field for the focusing channel is given by

$$\vec{B}^{\text{ext}}(x, y, s) = B_z(s) \hat{e}_z - \frac{1}{2} B_z'(s) (x \hat{e}_x + y \hat{e}_y) \quad (1)$$

and

$$\vec{B}^{\text{ext}}(x, y, s) = \vec{B}^{\text{ext}}(x, y, s + S), \quad (2)$$

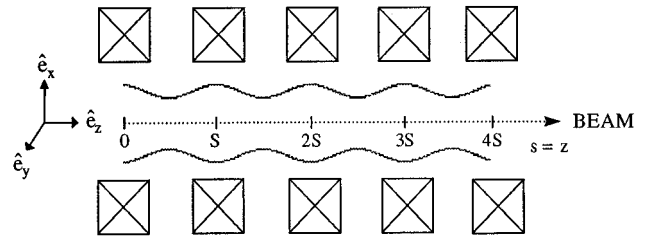


FIG. 1. Schematic of charged-particle beam propagation through a periodic solenoidal focusing channel, where the oscillatory curves illustrate the envelope for the rms-matched beam in the focusing channel.

where  $s=z$  is the axial coordinate,  $S$  is the fundamental periodicity length of the focusing field, and the prime denotes derivative with respect to  $s$ .

### A. Beam self fields

To derive the transverse equations of motion for individual test particles, we make the paraxial approximation which implies (a) the Budker parameter is small compared with unity, i.e.,  $q^2 N / m c^2 \ll 1$ , (b) the beam is thin compared with the lattice period  $S$ , and (c) the transverse kinetic energy is small compared with the axial kinetic energy, i.e.,  $v_x^2 + v_y^2 \ll v_z^2 \cong \beta_b^2 c^2$ . Here,  $N$  is the number of particles per unit axial length,  $m$  and  $q$  are the particle rest mass and charge, respectively,  $c$  is the speed of light in *vacuo*, and  $\vec{v}$  is the particle velocity. Furthermore, we assume that the beam is rms matched into the focusing channel and has the following density profile:

$$n_b(r, s) = \begin{cases} \hat{n}_b(s) + \delta \hat{n}_b(s) \left[ 1 - \frac{2r^2}{r_b^2(s)} \right], & \text{for } r < r_b(s), \\ 0, & \text{for } r > r_b(s), \end{cases} \quad (3)$$

where  $r = (x^2 + y^2)^{1/2}$  is the radial coordinate,  $r_b(s) = r_b(s + S)$  is the radius (core envelope) for the rms-matched beam,  $\hat{n}_b(s) = N / \pi r_b^2(s)$ , and  $\delta \hat{n}_b(s) = \delta N / \pi r_b^2(s)$  is a measure of nonuniformity in the beam density profile. The beam density profile is shown in Fig. 2. It is readily shown that the beam radius  $r_b(s)$  is related to the rms beam radius  $\langle r^2(s) \rangle^{1/2}$  by

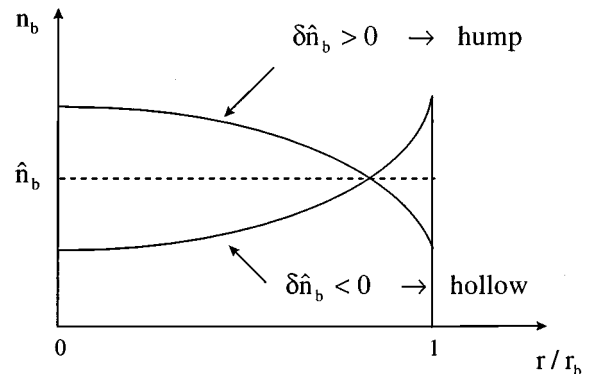


FIG. 2. Transverse density profiles described by Eq. (3).

$$\langle r^2(s) \rangle = N^{-1} \int dx dy n_b(r,s) r^2(s) = \frac{r_b^2(s)}{2g}, \quad (4)$$

where the geometric factor  $g$  is defined by

$$g = (1 - \delta \hat{n}_b / 3 \hat{n}_b)^{-1}. \quad (5)$$

For a beam with a uniform density profile,  $\delta \hat{n}_b(s) = 0$ , which corresponds to the KV equilibrium [13].

The self-electric and self-magnetic fields associated with the beam space charge and current are expressed as

$$\vec{E}^{(s)}(x,y,s) = - \left( \hat{e}_x \frac{\partial}{\partial x} + \hat{e}_y \frac{\partial}{\partial y} \right) \Phi^{(s)}(x,y,s), \quad (6)$$

$$\vec{B}^{(s)}(x,y,s) = \left( \hat{e}_x \frac{\partial}{\partial y} - \hat{e}_y \frac{\partial}{\partial x} \right) A_z^{(s)}(x,y,s), \quad (7)$$

where  $\partial/\partial s \equiv 0$  in the paraxial approximation, the scalar potential for the self-electric field is obtained by integrating Poisson's equation

$$\left( \frac{\partial^2}{\partial x^2} + \frac{\partial^2}{\partial y^2} \right) \Phi^{(s)} = -4\pi q n_b(r,s), \quad (8)$$

and the vector potential for the self-magnetic field is defined by

$$\vec{A}^{(s)}(x,y,s) = \beta_b \Phi^{(s)}(x,y,s) \hat{e}_z. \quad (9)$$

The solution to Poisson's equation (8) is

$$\Phi^{(s)}(r,s) = \begin{cases} -q(N + \delta N) r^2 / r_b^2(s) + q \delta N r^4 / 2 r_b^4(s), & \text{for } r \leq r_b(s) \\ -q(N + \delta N / 2) - 2qN \ln[r/r_b(s)], & \text{for } r > r_b(s). \end{cases} \quad (10)$$

### B. Determination of the rms-matched envelope

The radius for the rms-matched beam is determined from the envelope equation

$$\frac{d^2 r_b}{ds^2} + \kappa_z(s) r_b - \frac{gK}{r_b} - \frac{(4g\epsilon)^2}{r_b^3} = 0, \quad (11)$$

which is derived following the analysis by Sacherer [10]. In Eq. (11), the geometric factor  $g$  is defined in Eq. (5); the focusing parameter is defined by

$$\kappa_z(s) = \left[ \frac{qB_z(s)}{2\gamma_b \beta_b m c^2} \right]^2 = \kappa_z(s+S), \quad (12)$$

where  $\gamma_b = (1 - \beta_b^2)^{-1/2}$ ; the normalized beam perveance is defined by

$$K = \frac{2q^2 N}{\gamma_b^3 \beta_b^2 m c^2}; \quad (13)$$

and the rms emittance  $\epsilon$  is assumed to be constant and is defined by  $\epsilon = \epsilon_{\bar{x}} = \epsilon_{\bar{y}}$  and [10]

$$\epsilon_{\bar{x}} = (\langle \bar{x}^2 \rangle \langle \bar{x}'^2 \rangle - \langle \bar{x} \bar{x}' \rangle^2)^{1/2}, \quad (14a)$$

$$\epsilon_{\bar{y}} = (\langle \bar{y}^2 \rangle \langle \bar{y}'^2 \rangle - \langle \bar{y} \bar{y}' \rangle^2)^{1/2}. \quad (14b)$$

Here,  $\langle \rangle$  represents the ensemble average over the beam particle distribution, and the particle transverse displacement in the Larmor frame of reference,  $(\bar{x}, \bar{y})$ , is related to that in the laboratory frame of reference,  $(x, y)$ , by

$$\bar{x}(s) = x(s) \cos[\phi(s)] - y(s) \sin[\phi(s)], \quad (15a)$$

$$\bar{y}(s) = x(s) \sin[\phi(s)] + y(s) \cos[\phi(s)], \quad (15b)$$

with  $\phi(s) = \int_{s_0}^s \sqrt{\kappa_z(s)} ds$ .

In general, the solutions to the envelope equation (11) can exhibit both regular and chaotic behavior [3,8]. The present model describes the dynamics of an rms-matched beam whose radius corresponds to a periodic solution to the envelope equation (11). When the strength of the focusing field is moderate, Eq. (11) has a unique periodic solution with  $r_b(s) = r_b(s+S)$  [3].

For the case of an even focusing lattice with  $\kappa_z(s) = \kappa_z(-s)$ , it can be shown [3] that Eq. (11) is invariant under the time-reversal transformation  $(s, r_b) \rightarrow (-s, r_b)$ , and that the periodic solution  $r_b(s) = r_b(s+S)$  has the property  $r_b'(0) = 0$ . In this case, the rms-matched beam envelope can be determined numerically using a shooting method.

Figure 3 shows the periodic envelope for an rms-matched beam propagating through a periodically interrupted solenoidal focusing channel with the focusing parameter defined by the following periodic step function:

$$\kappa_z(s) = \begin{cases} \kappa_{z0}, & \text{for } -\eta/2 \leq s/S < \eta/2, \\ 0, & \text{for } \eta/2 \leq s/S < 1 - \eta/2, \end{cases} \quad (16)$$

where  $\eta$  is the filling factor. The vacuum phase advance for the particle motion in this lattice is given approximately by

$$\sigma_0 = \left[ S \int_0^s \kappa_z(s) ds \right]^{1/2} = (\eta S^2 \kappa_{z0})^{1/2}, \quad (17)$$

which is a measure of the strength of the average focusing field. The choice of system parameters in Fig. 3 corresponds to:  $\eta = 0.2$ ,  $S^2 \kappa_{z0} = 12.0$  ( $\sigma_0 = 88.8^\circ$ ), and  $SK/4\epsilon = 10$ . It is evident in Fig. 3 that  $r_b'(0) = 0$ , as expected for  $\kappa_z(s) = \kappa_z(-s)$ . Note also that the results shown in Fig. 3 are independent of  $g$  in terms of the scaled variables defined by  $s/S$ ,  $S^2 \kappa_z$ , and  $(4g\epsilon S)^{-1/2} r_b$ .

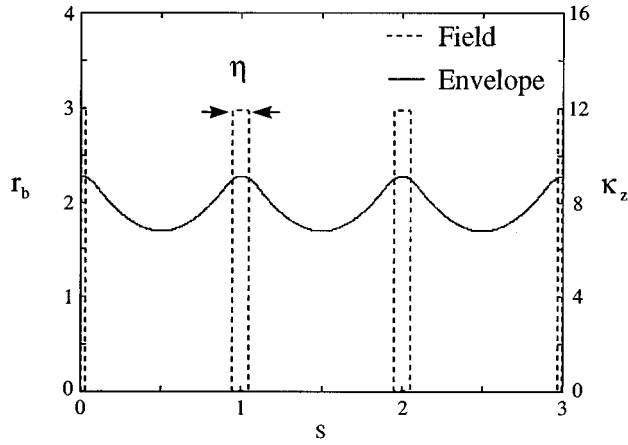


FIG. 3. Beam radius as a function of propagation distance  $s$  for an rms-matched beam propagating through a step-function lattice defined by Eq. (16). Here, the choice of system parameters corresponds to:  $\eta=0.2$ ,  $S^2\kappa_{z0}=12.0$  ( $\sigma_0=88.8^\circ$ ), and  $SK/4\epsilon=10$ . The horizontal and vertical axes  $s$ ,  $r_b$ , and  $\kappa_z$  are scaled by the multiplication factors  $S^{-1}$ ,  $(4g\epsilon S)^{-1/2}$ , and  $S^2$ , respectively.

### C. Transverse equations of motion

It can be shown that in the Larmor frame of reference, the transverse equations of motion for a test particle in the combined periodic solenoidal, and self-fields are expressed as

$$\frac{d^2x}{ds^2} + \kappa_z(s)x + \frac{q}{\gamma_b^3\beta_b^2mc^2} \frac{\partial}{\partial x} \Phi^{(s)}(x,y,s) = 0, \quad (18)$$

$$f_b(x,y,x',y',s=s_0) = \begin{cases} \frac{N-\delta N}{16\pi^2\epsilon_m^2} \delta(W-1) + \frac{\delta N}{8\pi^2\epsilon_m} H(W), & 0 \leq \delta\hat{n}_b \leq \hat{n}_b, \\ \frac{N-\delta N}{16\pi^2\epsilon_m^2} \delta(W-1) + \frac{2\delta N}{\pi r_b^2(s)} R^2 H(R^2) \delta(x') \delta(y'), & -\hat{n}_b < \delta\hat{n}_b \leq 0, \end{cases} \quad (20)$$

where  $R^2 = (x^2 + y^2)/r_b^2$ ,

$$W(x,y,x',y',s=s_0) = \frac{r^2}{r_b^2} + \frac{1}{16\epsilon_m^2} \times [(r_b x' - x r_b')^2 + (r_b y' - y r_b')^2], \quad (21)$$

$$H(x) = \begin{cases} 1, & 0 \leq x \leq 1, \\ 0, & \text{otherwise,} \end{cases} \quad (22)$$

and the maximum emittance  $\epsilon_m$  is defined by

$$\frac{\epsilon}{\epsilon_m} = \begin{cases} 1 - \frac{\delta\hat{n}_b}{3\hat{n}_b}, & \text{for } 0 \leq \delta\hat{n}_b \leq \hat{n}_b, \\ \left(1 + \frac{2\delta\hat{n}_b}{3\hat{n}_b} - \frac{\delta\hat{n}_b^2}{3\hat{n}_b^2}\right), & \text{for } -\hat{n}_b < \delta\hat{n}_b < 0. \end{cases} \quad (23)$$

$$\frac{d^2y}{ds^2} + \kappa_z(s)y + \frac{q}{\gamma_b^3\beta_b^2mc^2} \frac{\partial}{\partial y} \Phi^{(s)}(x,y,s) = 0, \quad (19)$$

where  $\Phi^{(s)}(x,y,s)$  is defined in Eq. (10), and the tilde over the variables  $x$  and  $y$  has been omitted. Heretofore, the variables  $x$  and  $y$  should be understood as the variables  $\tilde{x}$  and  $\tilde{y}$ , respectively.

For a uniform-density beam with  $\delta N=0$ , the equations of motion (18) and (19) are linear for the test particle in the beam interior with  $r \leq r_b(s)$ , but become nonlinear for the test particle outside the beam with  $r > r_b(s)$ . It is important to point out that for nonuniform-density beams, however, the equations of motion are always nonlinear, regardless of whether the test particle is inside or outside the beam. It will be shown in Sec. III that for beam propagation through a periodic solenoidal focusing channel, Eqs. (18) and (19) are generally nonintegrable and support chaotic solutions.

In the limit of a uniform solenoidal focusing channel with  $\kappa_z(s)=\text{const}$ , the rms-matched beam radius is constant. As a result, the equations of motion (18) and (19) are integrable. In this case, test particles have regular orbits and are always confined inside the beam envelope.

### D. The initial distribution

In the present test-particle model, an initial distribution function corresponding to the parabolic density profile defined in Eq. (3) has been derived and is expressed as

It is readily verified that  $n_b(x,y,s=s_0) = \iint f_b(x,y,x',y',s=s_0) dx' dy'$ . Moreover, the distribution function  $f_b$  has the property that it approaches the KV equilibrium distribution [13] continuously as  $\delta\hat{n}_b \rightarrow 0$ . Therefore, the beams under the present investigation are perturbed directly from the KV equilibrium, which is the only known Vlasov equilibrium for periodically focused intense charged-particle beams.

To summarize, equations (18) and (19) together with Eqs. (10), (11), and (20) form the basis for subsequent investigations of chaotic particle motion and halo formation in an rms-matched, space-charge-dominated beam propagating through a periodic solenoidal focusing channel.

## III. NUMERICAL RESULTS

In this section, we discuss results of a numerical study of the beam dynamics for the case of the step-function lattice described by Eq. (16). In the numerical study, the envelope equation (11) and the particle equations (18) and (19) are

solved simultaneously using a fourth-order Runge Kutta integrator. The initial conditions for the envelope equation (11) are chosen such that they yield the periodic beam envelope as described in Sec. II. Because  $y=0=y'$  is invariant, we choose the initial conditions  $y(0)=0=y'(0)$  in all of the analyses discussed in this section. Moreover, for all of the results presented in Figs. 4–6, 8, and 9, the phase space variables are scaled according to:

$$\begin{aligned} s &\rightarrow \frac{s}{S}, & x &\rightarrow \frac{x}{r_b(0)}, & y &\rightarrow \frac{y}{r_b(0)}, \\ x' &\rightarrow \frac{r_b(0)x'}{4\epsilon_m}, & \text{and } y' &\rightarrow \frac{r_b(0)y'}{4\epsilon_m}, \end{aligned} \quad (24)$$

where  $\epsilon_m$  is the maximum emittance defined in Eq. (23).

### A. Uniform-density profile

Although the equations of motion (18) and (19) have a simple form, the transverse beam dynamics exhibits rich behavior whenever space-charge effects become significant. This is illustrated in Fig. 4, where Poincare surface-of-section plots [11] are shown in the phase space  $(x, x')$  for both emittance- and space-charge-dominated uniform-density beams. The choice of the system parameters in Fig. 4 corresponds to:  $\eta=0.2$ ,  $S^2\kappa_{z0}=10.0$  ( $\sigma_0=81.0^\circ$ ),  $g=1.0$  ( $\delta\hat{n}_b=0$ ), and  $SK/4\epsilon=0.5$  for the case of an emittance-dominated beam in (a) and  $SK/4\epsilon=6.0$  for the case of a space-charge-dominated beam in (b). For each case shown in Fig. 4, 41 particles are loaded initially at  $s=0$  uniformly along the  $x$  axis from  $x=-2.0$  to  $2.0$ , and the initial conditions are indicated by the crosses. The Poincare map [12] is generated here by plotting the positions and momenta of the test particles as they pass through the lattice points  $s=1, 2, \dots, 2000$ .

Figure 4(a) shows a simple and regular phase-space structure for the case of an emittance-dominated beam. By contrast, Fig. 4(b) shows a rather complicated phase-space structure for the case of a space-charge-dominated beam, containing a mixture of regular orbits, nonlinear resonances, and chaotic layers. In Fig. 4(b), all of the test particles loaded initially inside the beam envelope have regular orbits, and these particles correspond to those in the KV distribution. However, because Eqs. (18) and (19) are *nonlinear* for  $r > r_b(s)$  and because the strength of the nonlinearity is proportional to  $SK/4\epsilon$ , the orbits of some of the test particles that cross the beam envelope become chaotic, i.e., *sensitive to initial conditions*. The chaotic particle orbits lie in the chaotic layers are bounded by the invariant tori known as KAM surfaces [12].

It should be emphasized that all of the test particles in the KV distribution will remain inside the beam envelope, despite the fact that the underlying equations of motion (18) and (19) are nonintegrable and support chaotic solutions for  $r > r_b(s)$ . As far as beam halo formation is concerned, it is important to identify the mechanisms by which the test particles initially in the perturbed KV distribution  $f_b$  defined in Eq. (20) enter the chaotic layer. This is the subject matter discussed in the remainder of this section.

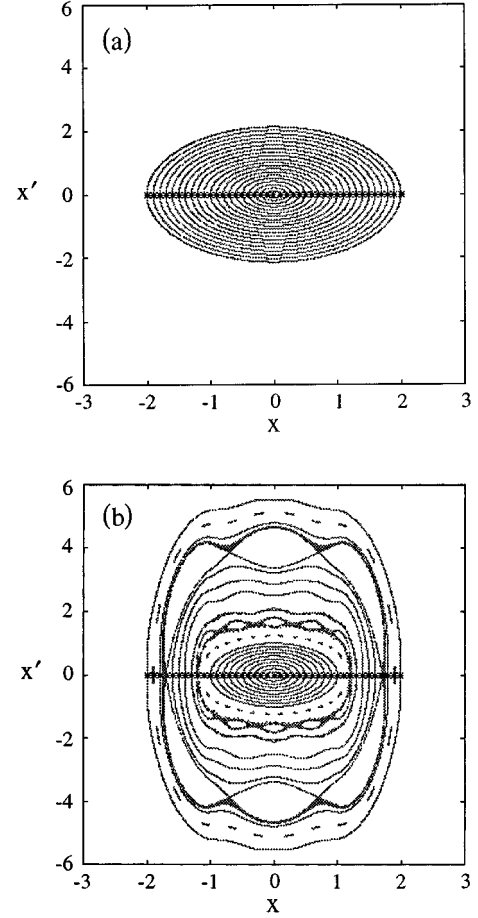


FIG. 4. Poincare surface-of-section plots in the phase space  $(x, x')$  for emittance- and space-charge-dominated beams propagating through 2000 lattice periods with uniform density profiles. The choice of the system parameters corresponds to:  $\eta=0.2$ ,  $S^2\kappa_{z0}=10.0$  ( $\sigma_0=81.0^\circ$ ),  $g=1.0$  ( $\delta\hat{n}_b=0$ ), and  $SK/4\epsilon=0.5$  for the case of an emittance-dominated beam in (a) and  $SK/4\epsilon=6.0$  for the case of a space-charge-dominated beam in (b).

### B. Hollow density profile

Figure 5 shows Poincare surface-of-section plots in the phase space  $(x, x')$  for a beam with a hollow density profile. The system parameters in Fig. 5 are:  $\eta=0.2$ ,  $S^2\kappa_{z0}=7.46$  ( $\sigma_0=70^\circ$ ),  $SK/4\epsilon=14$ , and  $\delta\hat{n}_b/\hat{n}_b=-0.1$  ( $g=0.96$ ) for case (a) and  $\delta\hat{n}_b/\hat{n}_b=-0.2$  ( $g=0.93$ ) for case (b). For every case shown in Fig. 5, 41 test particles are loaded initially on a circle defined by  $W(x, x', 0, 0)=1$  in the phase space, and the initial conditions are indicated by the crosses. Note that  $W=1$  is the maximum value achieved by any particle in the perturbed KV distribution  $f_b$ . The Poincare surface-of-section plots are generated here in the same way as in Fig. 4.

In Fig. 5, there is a pair of stable and unstable fixed points at the edge of the beam, i.e., at  $(x, x') \approx (1, 0)$  in the phase space. The unstable fixed point is located inside the beam, whereas the stable fixed point and associated island are located outside of the beam. Because of the symmetry in the underlying equations of motion (18) and (19), there is another pair of stable and unstable fixed points at  $(x, x') \approx (-1, 0)$ . These fixed points, which correspond to periodic solutions of the equations of motion (18) and (19), are induced by excessive space charge at the edge of the hollow

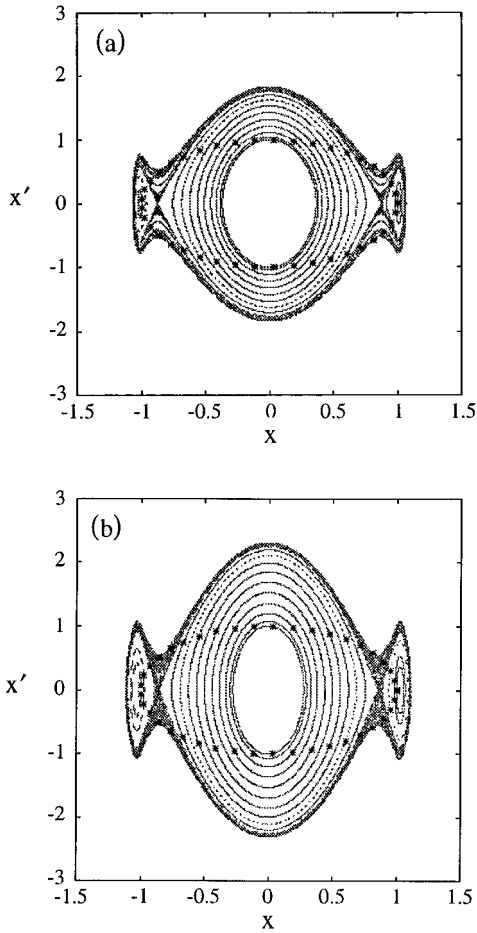


FIG. 5. Poincaré surface-of-section plots in the phase space  $(x, x')$  for a beam propagating through 2000 lattice periods with a hollow density profile. Here, the choice of system parameters corresponds to:  $\eta=0.2$ ,  $S^2\kappa_{z0}=7.46$  ( $\sigma_0=70^\circ$ ),  $SK/4\epsilon=14$ , and  $\delta\hat{n}_b/\hat{n}_b=-0.1$  ( $g=0.96$ ) for case (a) and  $\delta\hat{n}_b/\hat{n}_b=-0.2$  ( $g=0.93$ ) for case (b).

beam. Associated with the two unstable fixed points is a thin chaotic layer (separatrix), which occupies both the region with  $W < 1$  and the region with  $W > 1$  in the phase space. Particles in this thin chaotic layer can cross the beam envelope, forming a halo around a dense core of beam determined by  $W \leq 1$  in the phase space. Although the chaotic layer has a sizable excursion along the  $x'$  axis, it extends to  $x \approx \pm 1.1$  along the  $x$  axis. Therefore, the halo size in both examples shown in Fig. 5 is about 10% larger than the beam core radius. Moreover, because the chaotic layer is thin, the particle density in the halo region is expected to be very tenuous compared with that in the core region.

Although the Poincaré surface-of-section plots in Fig. 5 are obtained for beam propagation through a long focusing channel with 2000 lattice periods in order to show fine structures in the phase space, it should be emphasized that the process of halo formation occurs rapidly. Furthermore, as the density perturbations become larger, the width and size of the separatrix increase, leading to a more extended halo. This is illustrated in Fig. 6 with the choice of the system parameters corresponding to:  $\eta=0.2$ ,  $S^2\kappa_{z0}=12.0$  ( $\sigma_0=88.8^\circ$ ),  $SK/4\epsilon=10$ , and  $\delta\hat{n}_b/\hat{n}_b=-0.95$  ( $g=0.76$ ). The Poincaré surface-of-section plot in Fig. 6 is obtained for beam propa-

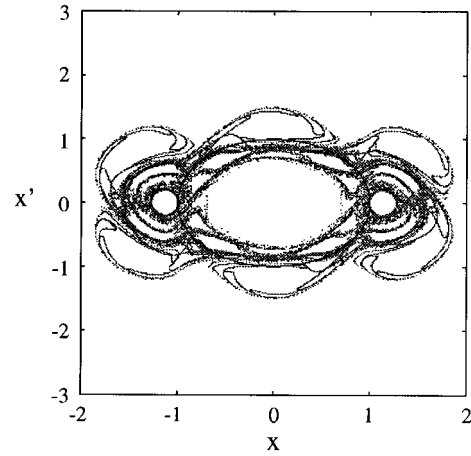


FIG. 6. Poincaré surface-of-section plots in the phase space  $(x, x')$  for a beam propagating through 20 lattice periods with a hollow density profile and 2000 test particles. Here, the choice of system parameters corresponds to:  $\eta=0.2$ ,  $S^2\kappa_{z0}=12.0$  ( $\sigma_0=88.8^\circ$ ),  $SK/4\epsilon=10$ , and  $\delta\hat{n}_b/\hat{n}_b=-0.95$  ( $g=0.76$ ).

gation through 20 lattice periods of the focusing field with 2000 test particles loaded initially on the circle  $W(x, x', 0, 0) = 1$ . The halo size in Fig. 6 is  $x_{\text{halo}} = 1.8$ , i.e., 1.8 times the beam core radius.

Shown in Fig. 7 as the dashed and bold solid curves are, respectively, examples of regular and chaotic trajectories for the same choice of system parameters shown in Fig. 6. In Fig. 7,  $s$  is scaled by the multiplication factor  $S^{-1}$ , and both  $x$  and  $\pm r_b$  are scaled by the multiplication factor  $(4g\epsilon S)^{-1/2}$ . The regular trajectory is initialized well inside the beam envelope with  $x' = 0$ , whereas the chaotic trajectory is initialized near the unstable fixed point with  $x' = 0$ . Also shown in Fig. 7 as the two solid curves is the periodic boundary ( $\pm r_b$ ) of the rms-matched beam. The chaotic tra-

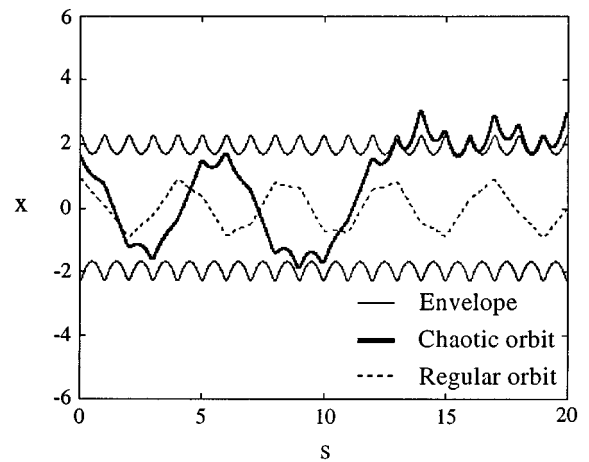


FIG. 7. Shown as the dashed and bold solid curves are, respectively, regular and chaotic trajectories for the same choice of system parameters shown in Fig. 6. Also shown as the two solid curves is the periodic boundary of the rms-matched beam. The chaotic trajectory intersects the beam envelope approximately at the thirteenth period of the focusing channel. Here,  $s$  is scaled by the multiplication factor  $S^{-1}$ , and both  $x$  and  $\pm r_b$  are scaled by the multiplication factor  $(4g\epsilon S)^{-1/2}$ .

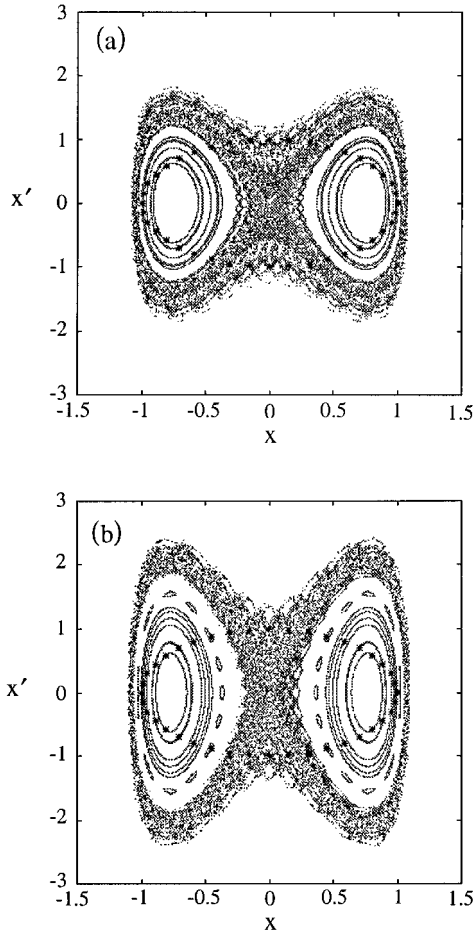


FIG. 8. Poincaré surface-of-section plots in the phase space  $(x, x')$  for a beam propagating through 2000 lattice periods with a hump density profile. Here, the choice of systems parameters corresponds to:  $\eta=0.2$ ,  $S^2\kappa_{z0}=7.46$  ( $\sigma_0=70^\circ$ ),  $SK/4\epsilon=14$ , and  $\delta\hat{n}_b/\hat{n}_b=0.1$  ( $g=1.03$ ) for case (a) and  $\delta\hat{n}_b/\hat{n}_b=0.2$  ( $g=1.07$ ) for case (b).

jectory intersects the beam envelope approximately at the thirteenth period of the focusing channel.

### C. Hump density profile

Figure 8 shows Poincaré surface-of-section plots in the phase space  $(x, x')$  for a beam with a hump-density profile. The system parameters in Fig. 8 are:  $\eta=0.2$ ,  $S^2\kappa_{z0}=7.46$  ( $\sigma_0=70^\circ$ ),  $SK/4\epsilon=14$ , and  $\delta\hat{n}_b/\hat{n}_b=0.1$  ( $g=1.03$ ) for case (a) and  $\delta\hat{n}_b/\hat{n}_b=0.2$  ( $g=1.07$ ) for case (b). As in Figs. 5 and 6, 41 particles are loaded initially on a circle defined by  $W(x, x', 0, 0, 0)=1$  in the phase space, and the initial conditions are indicated by the crosses in Fig. 8.

Figures 8(a) and 8(b) exhibit qualitatively the same phase-space structure; that is, both show two stable fixed points at  $(x, x')=(\pm 0.85, 0)$  and an unstable fixed point at the origin  $(x, x')=(0, 0)$ . Particles initialized near the unstable fixed point assume chaotic motion that result in the formation of a halo. By comparing the two cases shown in Fig. 8, it is evident that an increase in density nonuniformity leads to an increase in the total (edge) beam emittance, but does not lead to an appreciable increase in the halo size. In both cases, the

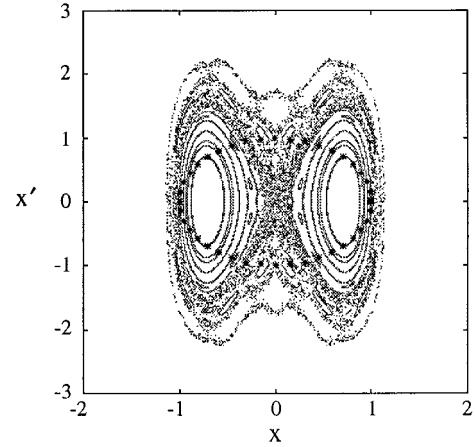


FIG. 9. Poincaré surface-of-section plot in the phase space  $(x, x')$  for a beam propagating through 2000 lattice periods with a hump density profile. Here, the choice of systems parameters corresponds to:  $\eta=0.2$ ,  $S^2\kappa_{z0}=12.0$  ( $\sigma_0=88.8^\circ$ ),  $SK/4\epsilon=10$ , and  $\delta\hat{n}_b/\hat{n}_b=0.4$  ( $g=1.24$ ).

halo extends to about 1.15 times the beam radius.

Unlike beams with hollow density profiles, the size of the halo around a beam with a hump density profile does not change appreciably as the density nonuniformity is increased. This is evident by comparing the case with a hollow density profile shown in Fig. 6 with the case with a hump density profile beam shown in Fig. 9.

## IV. CONCLUSIONS

The dynamics of continuous space-charge-dominated beams propagating through a periodic solenoidal focusing channel has been studied using a test-particle model. The studies were carried out in the regime where the beam is assumed to be rms matched into the focusing channel but have a nonuniform density profile transverse to the direction of beam propagation. It was shown that nonlinearities in the self-fields induce chaotic particle motion and beam halo formation.

For beams with hollow density profiles (i.e., with low densities on the beam axis and high densities at the beam edge), it was found that excessive space charge at the edge of the beam induces two pairs of stable and unstable period-one orbits (i.e., two pairs of stable and unstable fixed points of the Poincaré map) in the vicinity of the beam core envelope, and that the chaotic layer associated with the unstable period-one orbits allows particles to escape from the core to form a halo. The halo was found to be bounded by a KAM surface. The ratio of halo to beam core envelope, which, depending on system parameters, can be up to a value of 1.8, was determined numerically.

On the other hand, for beams with hump density profiles (i.e., with high densities on the beam axis and low densities at the beam edge), it was found that excessive space charge on the beam axis induces an unstable fixed point on the axis and two stable period-one orbits (i.e., two stable fixed points of the Poincaré map) off the axis inside the beam. In this

case, the mechanism of beam halo formation was identified with the chaotic layer associated with the unstable fixed point on the beam axis. The ratio of halo to beam core envelope for a beam with a hump density profile was found to be less than that for a beam with a hollow density profile, for, otherwise, the same choice of system parameters.

It should be emphasized that for rms-matched beams propagating through a uniform solenoidal focusing channel, test particles do *not* exhibit either chaotic behavior or beam

halo formation, because the equations of motion are integrable for an arbitrary density profile with axisymmetry.

#### ACKNOWLEDGMENTS

This work was supported by the U.S. Department of Energy, Office of High Energy and Nuclear Physics, Grant No. DE-FG02-95ER-40919 and by the Air Force Office of Scientific Research, Grant No. F49620-94-1-0374.

- 
- [1] *Space Charge Dominated Beams and Applications of High Brightness Beams*, edited by S. Y. Lee, AIP Conf. Proc. No. 377 (AIP, New York, 1996).
  - [2] J. S. O'Connell, T. P. Wangler, R. S. Mills, and K. R. Crandall, in Proc. 1993 Particle Accel. Conf. edited by S. T. Corneliussen (IEEE Service Center, Piscataway, New Jersey, 1993), Vol. 5, p. 3657.
  - [3] C. Chen and R. C. Davidson, Phys. Rev. Lett. **72**, 2195 (1994); Phys. Rev. E **49**, 5679 (1995).
  - [4] Q. Qian, R. C. Davidson, and C. Chen, Phys. Plasmas **1**, 3104 (1994); Phys. Plasmas **2**, 2674 (1995).
  - [5] L. M. Lagniel, Nucl. Instrum. Methods Phys. Res. **345**, 1516 (1994).
  - [6] R. L. Gluckstern, Phys. Rev. Lett. **73**, 1247 (1994).
  - [7] C. Chen and R. A. Jameson, Phys. Rev. E **52**, 3074 (1995).
  - [8] S. Y. Lee and A. Riabko, Phys. Rev. E **51**, 1609 (1995).
  - [9] C. Chen, in *Space Charge Dominated Beams and Applications of High Brightness Beams* (Ref. [1]), p. 169.
  - [10] F. J. Sacherer, IEEE Trans. Nucl. Sci. **NS-18**, 1105 (1971).
  - [11] S. Yu, S. Eylon, E. Henestroza, and D. Grote, AIP Conf. Proc. **377**, 134 (1996).
  - [12] A. J. Lichtenberg and M. A. Leiberman, *Regular and Chaotic Dynamics*, 2nd ed. (Springer-Verlag, New York, 1992).
  - [13] I. M. Kapchinskij and V. V. Vladimirkij, in *Proceedings of the International Conference on High Energy Accelerators* (CERN, Geneva, 1959), p. 274.